Honors Theses

Honors College

5-2024

Measurement of the Branching Fraction of Y(4S), B^0B^0 at BABAR

Daniel B. Johnson

Measurement of the Branching Fraction of $\Upsilon(4S) \to B^0\overline{B^0}$ at BABAR
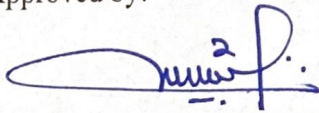
By

Daniel Johnson

A thesis submitted in partial fulfillment of the requirements of the Honors College at

the University of South Alabama and the Bachelor of Sciences

in the Physics Department

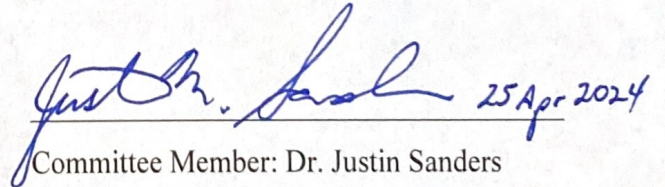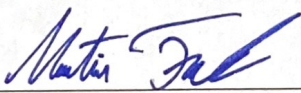University of South Alabama

Mobile, AL

May 2024

Approved by:

_____ 4/25/2024

Mentor: Dr. Romulus Godang

_____ 25 Apr 2024

Committee Member: Dr. Justin Sanders

_____ 4/25/2024

Committee Member: Dr. Martin Frank

_____

Honors Dean, Dr. Doug Marshall

ABSTRACT

Based on a data sample of 476 million $B\bar{B}$ pairs collected at the $Y(4S)$ resonance with the BABAR detector at the PEP-II asymmetric-energy B-Factory at SLAC National Accelerator Laboratory, we measure the branching fraction of the decay $Y(4S) \rightarrow B^0\overline{B^0} \equiv f_{00}$. Using a partial reconstruction technique, the B-mesons are reconstructed from the decay $\overline{B^0} \rightarrow D^{*+}\ell^-\nu_\ell$ the lepton can be either an electron or a muon. The D^{*+} meson is detected through the soft pion (π) from its decay $D^{*+} \rightarrow D^0\pi^+$, where the D^* four-momentum is measured through the soft pion. The partial reconstruction technique allows us to get better statistical precision in the measurement of the branching fraction of $Y(4S) \rightarrow B^0\overline{B^0}$. This study measures the branching fraction of the decay $Y(4S) \rightarrow B^0\overline{B^0}$ to be $f_{00} = 0.485 \pm (0.007)_{Stat} \pm (0.004)_{syst}$ where the first uncertainty is statistical and the second is systematic.

Dedication

This work is dedicated to Nicole and Jaysn Johnson for being amazing parents who have always supported my love of Physics.

Acknowledgements

I would like to thank Dr. Romulus Godang, who made this work possible by providing the resources, guidance, and support needed for the past three years for both the research and writing processes.

I also want to give thanks to the Deans of the USA Honors College during my time as an undergraduate, Dr. Kathy Cooke and Dr. Doug Marshall. Their support over the years has been an invaluable asset.

Thanks to Dr. Martin Frank and Dr. Justin Sanders, members of my Thesis Committee, whose experience assisted in the making of this work into a complete project.

And to everyone who has given encouragement and aid on this project, a most sincere thank-you.

Contents

List of Figures

List of Tables

Chapter 1

Introduction

The field of Physics is a large and growing discipline that covers the basic laws that govern the known material world. Particle Physics, or High Energy Physics, specifically investigates the interactions and behaviors of subatomic particles and is a rapidly growing frontier of research. From the last few decades of research, a model has arisen that encompasses the interactions of such sub-atomic particles known as the Standard Model. The Standard Model, as a theory, explains the interactions of sub-atomic particles composed of some number of elementary particles; however, there remain several theorized and observed interactions that do not yet fit into the Standard Model. From the first theory of the atom, to understanding the structure of the atom's nucleus being composed of smaller particles known as protons and neutrons, all the way down to the current elementary particles, such as the electron, Particle Physics has set out to explain the most basic interactions of the building blocks of reality.

Particle Physics started to gain traction throughout the 20th century. In the early 20th century, the atomic model had gone through multiple revisions as more discoveries of the atomic structure came to light ending with Schrodinger's Quantum model in 1926. With the Quantum model the particles that compose the atom were known as protons, neutrons, and electrons. By 1932 Carl Anderson had seen a particle path in the cloud chamber that had the mass of an electron but moved as if it had a positive charge discovering the existence of antimatter composed of antiparticles. Following the discovery of these new particles, detection techniques advanced leading to hundreds of strongly interacting particles and their interactions being discovered and catalogued by the late 1960's. In the early 1970's the Standard Model was introduced as the main theory for describing the elementary particles and how they interact with each other. From the Standard Model it is seen that most particles are not fundamental but as combinations of elementary particles interacting together. The electron is currently understood as an elementary particle but once the nucleus of the atom was believed to be elementary but was comprised of protons and neutrons which in turn were further comprised of elementary particles known as quarks. Similarly to the electron, quarks are currently understood to be elementary particles. The base theory behind the Standard Model is that bulk matter is comprised of the six quarks and six antiquarks, forming hadrons, and the six leptons and six antileptons. Furthermore, the Standard Model can be broken up into two sections, the particles and their properties and the force and their interactions between the particles.

1.1 Particle Classification

As the Standard Model was being put together it became clear that the six quarks and their respective antiquarks should be classified within "families." The order of the quarks goes in the direction of increasing mass and are separated into three families. The family of low mass quarks are the up (u) quark and the down (d) quark. Followed by the second family of approximately one to three orders of magnitude more massive quarks are the strange (s) quark and charm (c) quark. The third and final family contains the most massive quarks, the bottom (b) quark and the top (t) quark. Alongside mass, particles have fundamental properties that when taken all together uniquely classify a particle. Three important fundamental properties used in classifying particles are mass, spin, and electric charge. Mass and charge are commonly understood phenomena; however, spin is a much more esoteric phenomenon. Spin is the intrinsic angular momentum of particles, unfortunately there is not an intuitive explanation for what this intrinsic angular momentum is. The original experiment that expresses the property of spin involved firing a beam of, typically, electrically neutral atoms through a magnetic field in turn splitting the beam into two separate curved paths. The experiment indicated that particles have an intrinsic magnetic dipole moment that is analogous to an intrinsic angular momentum which will take on distinct quantized values. It was originally theorized that the particle did intuitively spin along some central axis similarly to a top but was dismissed when it was discovered for that to be the case the "surface" of an electron would have a tangential velocity exceeding the speed of light.

The fundamental properties are important in characterizing particles. As previously mentioned, each quark has different mass values, but each quark also has a spin of $\frac{1}{2}$ and some fractional electric charge. To see this fractional charge take a hadron such as the proton consisting of two (u) quarks and one (d) quark, the proton has a positive fundamental electrical charge of $+e$, one positive electron charge. For the two (u) quarks and one (d) quark to reach $+e$ charge for the proton by following conservation of charge the (u) quark has two-thirds the positive electron charge $+\frac{2}{3}e$ and the (d) quark has one-third the negative electron charge $-\frac{1}{3}e$. The hadrons formed by the quarks can only form in combinations of the quarks where the quarks obey physical conservation laws, such as, the conservation of electric charge, in turn leading to hadrons having only integer charges. Table 1.1 records the fundamental properties of mass and charge of the six quarks; the spin of all six quarks is $\frac{1}{2}$ [1].

Table 1.1: The six quarks.

Quark	Charge (e)	Rest Mass (MeV/c^2)
u	$+\frac{2}{3}$	$1.9 - 2.7$
d	$-\frac{1}{3}$	$4.5 - 5.2$
s	$-\frac{1}{3}$	$90 - 102$
c	$+\frac{2}{3}$	$1250 - 1290$
b	$-\frac{1}{3}$	$4160 - 4210$
t	$+\frac{2}{3}$	173000

As previously mentioned, hadrons are comprised of combinations of quarks, specifically hadrons are comprised of two or three quarks. A three-quark combination is a baryon meaning heavy in Greek and a two-quark combination is called a meson meaning middle in Greek. The most familiar baryons would be protons (uud) and neutrons (udd). A few examples of baryons and their properties are listed in Table 1.2 [1].

Table 1.2: A few examples of baryons.

Baryon	Symbol	Quark Content	Mass (MeV/c^2)
Proton	p	uud	938.3
Neutron	n	udd	939.6
Lambda	Λ^o	uds	1116
Sigma-Plus	Σ^+	uus	1189
Xi	Ξ^0	uss	1315

It should be noted that there are no two-quark combinations that can be formed to give the resulting meson an integer charge due to the fractional charge of the quarks. Every quark has a related antiquark that is identical except for its electrical charge. In Table 1.1 for each quark there is an implied antiquark with the charge's sign flipped. These antiquarks can in turn pair with quarks, that it is not related to, to form a quark-antiquark pair with a whole integer charge. By definition, a meson is a quark-antiquark pair containing one quark and one antiquark. A few examples of mesons and their properties are listed in Table 1.3 [1]; antiquarks are denoted with a bar above the respective quark symbol.

The final part of the classification of particles in the Standard Model is the tabulation of the leptons meaning light in Greek. Similarly to quarks the leptons have spin $\frac{1}{2}$, yet the leptons themselves hold integer charge instead of fractional charge. The familiar lepton is the electron, but alongside the electron (e) are the two heavier leptons the muon (μ) and the tau (τ) particle each in the first, second, and third family, respectively. The other three leptons are the respective neutrino to each previous lepton: the electron-neutrino (v_e), muon-neutrino (v_μ), and tau-neutrino (v_τ). The neutrinos have a finite mass that is approximately close to zero and have a neutral electric charge but are measurable by conservation of lepton number. Similarly to the quarks each lepton has an anti-lepton with the same mass but opposite charge. The leptons and their properties [1] are listed in Table 1.4.

Table 1.3: A few examples of mesons.

Particle	Quarks	Antiparticle	Quarks	Mass (MeV/c^2)
π^+	$u\bar{d}$	π^-	$\bar{u}d$	139.57
K^0	$d\bar{s}$	$\bar{K}^0$	$\bar{d}s$	497.61
D^+	$c\bar{d}$	D^-	$\bar{c}d$	1869.7
D^0	$c\bar{u}$	$\bar{D}^0$	$\bar{c}u$	1864.8
B^+	$u\bar{b}$	B^-	$\bar{u}b$	5279.3
B^0	$d\bar{b}$	$\bar{B}^0$	$\bar{d}b$	5279.7

Table 1.4: The three lepton families.

Lepton	Charge (e)	Mass (MeV/c^2)
e	-1	0.511
ν_e	0	$< 8 \times 10^{-7}$
μ	-1	105.7
ν_μ	0	< 0.19
τ	-1	1777
ν_τ	0	< 18.2

1.2   Fundamental Interactions

The fundamental particles hold intrinsic properties, but beyond their intrinsic properties the Standard Model studies the interactions between these particles. The known fundamental interactions of nature are the four fundamental forces which hold particles together to create larger structures. From weakest to strongest the four fundamental forces are the gravitational, electromagnetic, weak nuclear, and strong nuclear force. Not only do these forces depend on the interactions between particles but also the distance between them. Gravity is the weakest of the fundamental forces, yet it works over the largest distances leading to it dominating in the macroscopic world by keeping the planets spherical and holding planets in orbit of their home star. Despite gravity's apparent strength at large distances, a small magnet can easily overcome gravity and attract a piece of metal

against the direction of gravity. In the microscopic world gravity plays a small role in the behavior of particles.

To better quantify the strengths of these four fundamental forces with respect to each other, it is prudent to define such strength in terms of a dimensionless constant known as the coupling constant. The coupling constants and the respective force carrier [1] are listed in Table 1.5.

Table 1.5: Relative strengths of coupling constants and force carrier particles.

Interaction	Strong	Electromagnetic	Weak	Gravity
Mediator	g (Gluons)	γ (Photon)	W^+, W^-, Z^0 (Bosons)	G (Graviton*)
Coupling Constant	α_s	α	α_w	α_g
Relative Strength	1	$\dfrac{1}{137}$	10^{-5}	10^{-38}

*Postulated

Each of the four fundamental forces obey different laws for their interactions between different particles. Both the gravitational and electromagnetic forces obey distance inverse square laws, thus they act over infinite distances. The weak and strong nuclear forces, however, only act over microscopic distances in the atom. The atomic nucleus is on the order of 10^{-15} meters and is held together by the strong nuclear force despite the protons electromagnetically repelling each other. The atom itself is on the order of 10^{-10} meters and is dominated by the electromagnetic force. The Standard Model only includes the strong nuclear, weak nuclear, and electromagnetic forces due to gravity being significantly weaker than the other forces and the lack of an accepted theory of quantum gravity.

These forces and their interactions lead to particles decaying into lighter and more stable particles. Particle physicists follow the Standard Model and experimentally determine the laws that these particle decays follow. A proton is effectively stable and will not decay in any reasonable time frame, if at all, but a neutron is not stable and will decay into a proton, electron, and anti-electron neutrino.

Particles can also have multiple decay paths and as such will not always decay into the same lighter particles called daughter particles. The parent particle, the particle that originally decays, can have multiple sets of daughter particles called a decay channel and there is a probability associated with each respective decay that the parent particle can take called a decay mode. As an example, the baryon Λ^o has multiple decay modes, one decay mode has lambda decaying into a proton (p) and a negatively charged pion (π^-)

$$\Lambda^o \to p\pi^-$$

with another decay mode into a neutron (n) and a neutral pion (π^0).

$$\Lambda^o \to n\pi^0$$

These two decay modes have a percent probability of occurring from the Λ^o particle known as a branching fraction. The first decay has a branching fraction of 0.641 ± 0.005 and the second decay has a branching fraction of 0.359 ± 0.005 [1]. This project aims to measure a precise branching fraction of the decay channel $Y(4S) \to B^0\overline{B^0}$ also known as f_{00}.

Chapter 2

The BABAR Detector

The BaBar Detector's at the Standford Linear Accelerator Center (SLAC) main purpose is to study the CP asymmetries in the decays of neutral B mesons. The Babar Detector is primed to study the collisions of electron and position beams at the $Y(4S)$ resonance with two beams of unequal energy. To achieve collisions of asymmetric electron and positron beams the collider positron electron project-II (PEP-II) is set with two rings, in one ring there is an electron beam with an energy of 9 GeV and in the second there is a positron beam with an energy of 3.1 GeV [2,3]. For the injection of the particle beams into the collider the SLAC linear accelerator or linac is used. The PEP-II collider has a luminosity of $\mathcal{L} = 3 \times 10^{33}$ cm^{-2}s^{-1} due to the lifetimes of the B mesons being relatively short, this high luminosity will provide enough B mesons to be measured [4]. The luminosity is the number of events detected over a period of time across some cross-sectional area. At the point of collision for the e^+e^- beams inside the Babar detector the center of mass energy for the $Y(4S)$ resonance will be 10.58 GeV. Figure 2.1 shows the layout of SLAC and the PEP-II accelerator into the Babar detector.
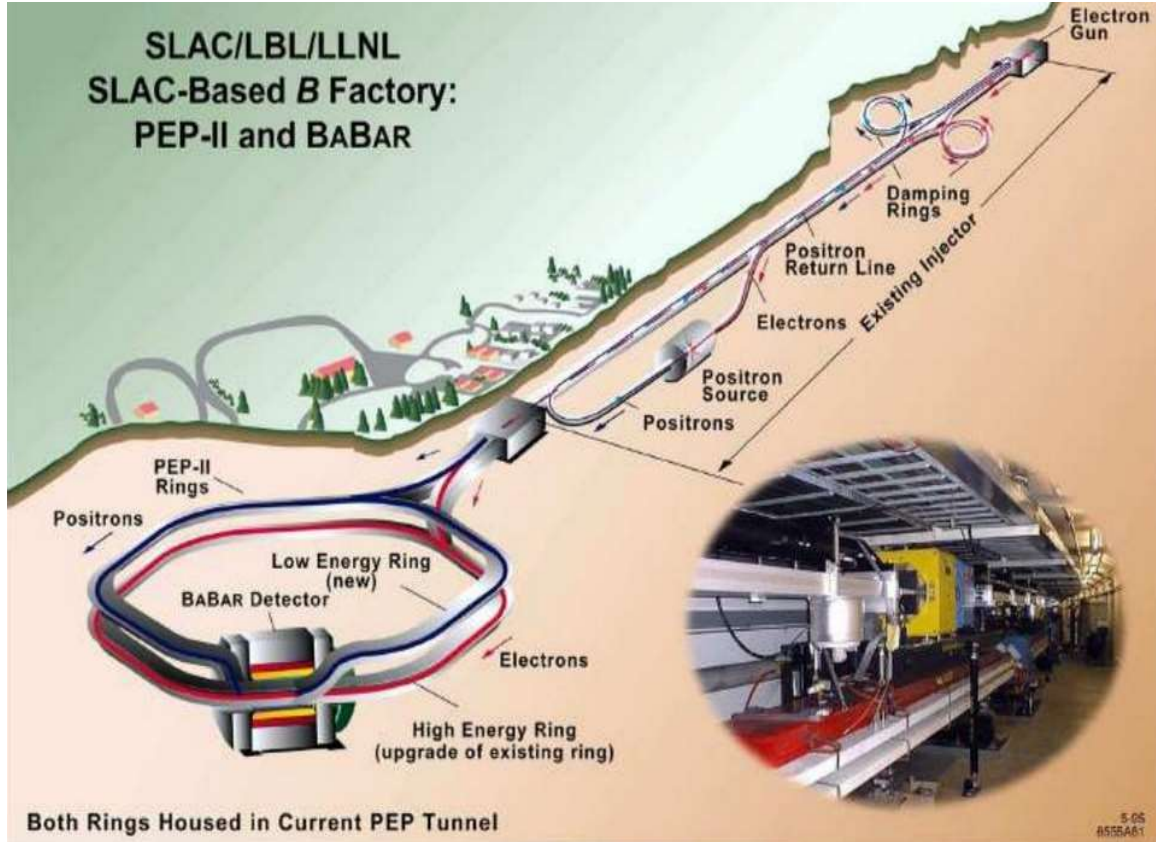
Figure 2.1: PEP-II accelerator and SLAC Linac.

The asymmetric collision of the electron and positron beams leads to the produced decay products to having a velocity along the direction of the e^- beam instead of being produced near rest. With this directionality the hadronic jets from the quarks and gluons will spread conically outwards after collision. Following, the B mesons will travel mostly along the z-axis such that the decay time difference will be measured due to the difference in their z-components of their decay positions.

The Babar detector itself holds a variety of segments that altogether measure the properties of the particles that come for the decay chain of the e^+e^- beam collision and the subsequent

decay of the $\Upsilon(4S)$ particle. By measuring these properties and matching these quantities with the Standard Model the particles can be classified and the appropriate data can be assigned and studied. The segments of interest here will be the silicon vertex tracker (SVT), drift chamber (DCH), CsI calorimeter (EMC), Cherenkov detector (DIRC), and the instrumented flux return (IFR) [5]. After collision, the daughter particles will fly through the detector's segments in the above listed order. Figure 2.2 shows the Babar detector alongside its segments.

Figure 2.2: BABAR Detector and its segments

2.1   The Silicon Vertex Tracker

The SVT's primary function is to measure the precise position of a particle's charged track left behind as the charged particle travels through the SVT. That is to say the SVT measures
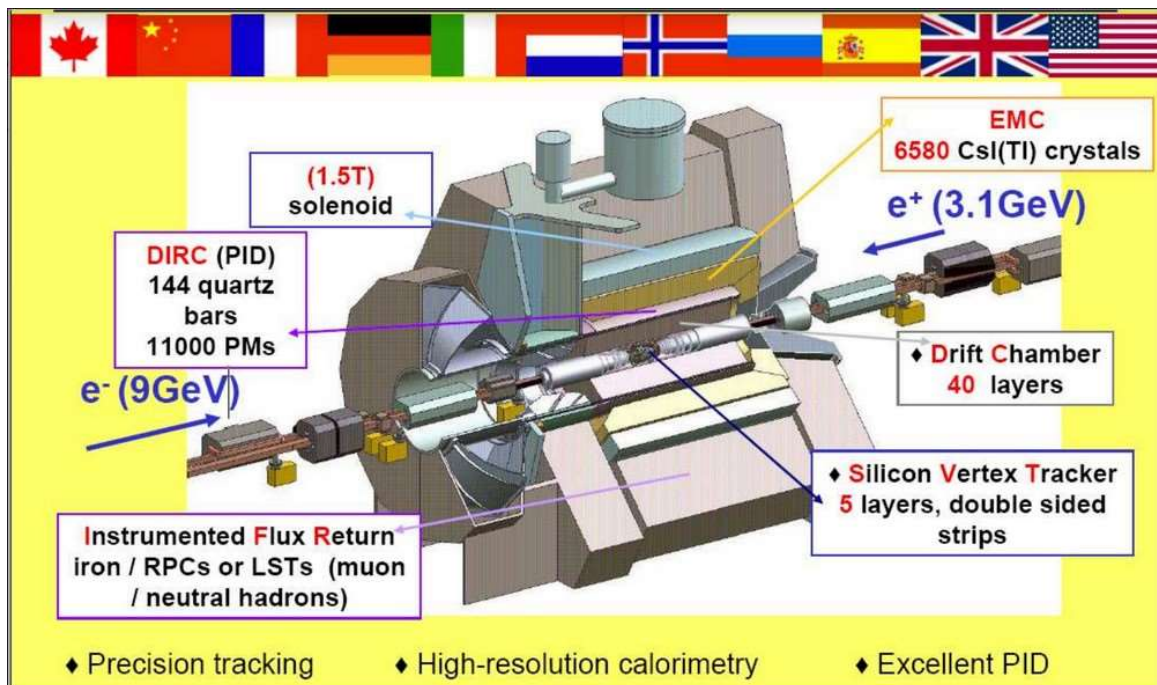
a charged particle at multiple points as it flies through "creating" a path the particle follows. Should a charged particle be of low energy it will only appear within the SVT and never reach the following segment. As previously mentioned with the positions of decays the time between two decays can be determined, thus the main benefit of the SVT is to determine when each measured decay occurs with respect to each other [5].

To measure as many of the charged tracks the active parts of the SVT was built around the polar angle of 20.1° and 150.2° due to the asymmetric nature of the collision of the e^+e^- beams. The SVT itself is comprised of five concentric cylindrical layers of double-sided silicon detectors with 90° stereo. These layers are further divided into individual modules with the first three layers having six detector modules in a traditional barrel structure and the last two having 16 and 18 detector modules, respectively. The SVT will have 340 silicon detectors within all the detector modules covering a total surface area of $1\ m^2$ with approximately 150,000 readout channels [5].

2.2   The Drift Chamber

The drift chamber is similar to the SVT in that it measures the position of the charged particles that travel through it. However, the DCH works at greater efficiency in track reconstruction for particles that have a transverse momentum greater than $100\ \mathrm{MeV/c}$ than the SVT. A charged particle with a transverse momentum less than $100\ \mathrm{MeV/c}$ will not be measured by the DCH since it never reaches past the SVT. The DCH itself provides 40 measurements of the spatial location of each charged particles track leading to excellent spatial and momentum resolutions of particle decays when paired with the SVT [5].

The DCH was made with a small-cell cylindrical design to minimize the drift time and a fast and highly pipelined design for the front-end electronics to reduce deadtime. Due to the asymmetric collisions of the e^+e^- beams the forward direction of the DCH is built with less materials in the way of particles traveling through it to optimize the distance a charged particle can travel through it. The DCH is comprised of multiple drift cells that are arranged into ten superlayers of four layers each. There are three types of superlayers where they alternate between the three types: axial (A) and stereo(U, V) in that order [5].

Further the performance of the DCH was evaluated by measuring the cosmic rays that naturally passed through the operational SVT and DCH. From the cosmic particle passing through the chamber the total energy loss from the particles traveling through the DCH to determine the specific energy loss (dE/dx) deposited within the detector to be calibrated for the e^+e^- beam collisions. dE/dx is the energy lost over some distance travelled by a charged particle from ionization as it travels through matter. The specific energy loss deposited within the detector was measured against the momenta of the traveling particle to find the expected resolution for the specific energy loss of 7%. Figure 2.3 shows the measurements of dE/dx and the momentum of the particles used to determine the actual resolution of the DCH to be 7.5% which is to be expected [6].
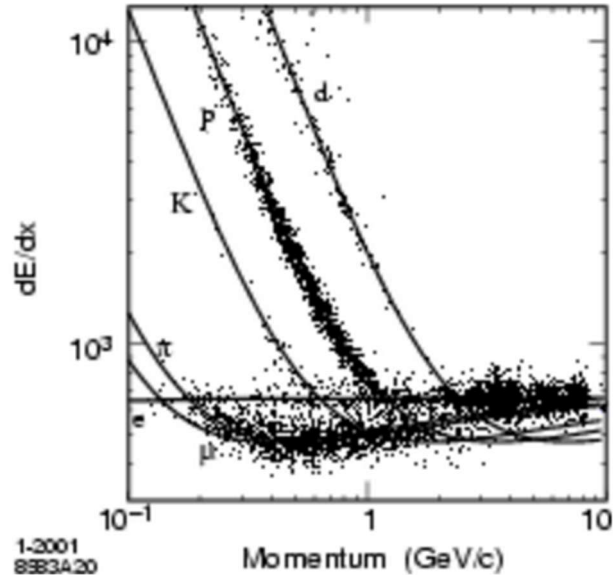
Figure 2.3: Measurement of dE/dx against the momenta of the particles through the DCH [6].

2.3 The Cherenkov Detector

The Cherenkov detector is devoted to particle identification by using the internal reflected Cherenkov light given off by the particles as they pass through the DIRC. Cherenkov radiation arises from protons and electrons that pass through a dielectric medium faster than light can travel through the same medium which will then emits light. The DIRC in the Babar detector is specifically excellent at detecting and identifying kaons whose momenta extend to ~ 2.0 GeV/c, and for higher momenta from rare B meson decay chains. Simultaneously, the DIRC is capable of distinguishing from pions and kaons up to ~ 4.0 GeV/c at large dip angles in the laboratory frame. This is necessary to distinguish between the two B meson decays $B^o \rightarrow \pi^+\pi^-$ and $B^o \rightarrow K^+\pi^-$. The final process of the

DIRC is to identify muons in the momentum range below 750 MeV/c due to inefficiencies in the IFR [5].

The base idea for the DIRC is that the magnitude of angles is kept consistent after reflection from a flat surface. With this idea in mind the radiators within the DIRC are made of synthetic fused silica molded into a long and thin rectangle henceforth referred to as a bar. The light that travels through the entirety of a bar to the instrumental end of the component will enter a standoff box which is an expansion region filled with water. At the exit of the bar there is a fused silica wedge that will reflect the light to photomultiplier tubes further surrounded by reflectors to capture light that would otherwise have escaped. The DIRC has 12 hermetically sealed containers specifically for the bars known as bar boxes that each has 12 bars arranged into the 12-sided polygonal barrel leading to a total of 144 bars within the DIRC. Figure 2.4 is the DIRC's main components and its support structure [6].
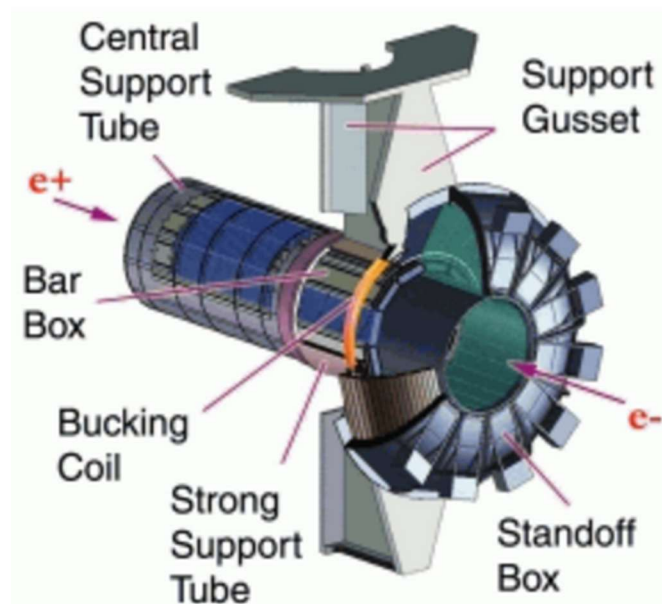
Figure 2.4: The schematic of the DIRC main components and the support structure within the Babar Detector [6].

The DIRC has been operating within the expected parameters of the Monte Carlo simulations. Figure 2.5 shows the signals detected by the photomultiplier tubes within the DIRC from a typical di-muon event: $e^+e^- \rightarrow \mu^+\mu^-$. From Figure 2.5 the left image shows the signal within a $\pm 300\ ns$ trigger while the right image shows the signals in the expected $8\ ns$ trigger for Cherenkov photon arrival time within the DIRC. The background comes from low energy photons that originate from the PEP-II machine hitting the standoff and has been mitigated by lead shielding installed around beam line components [6].
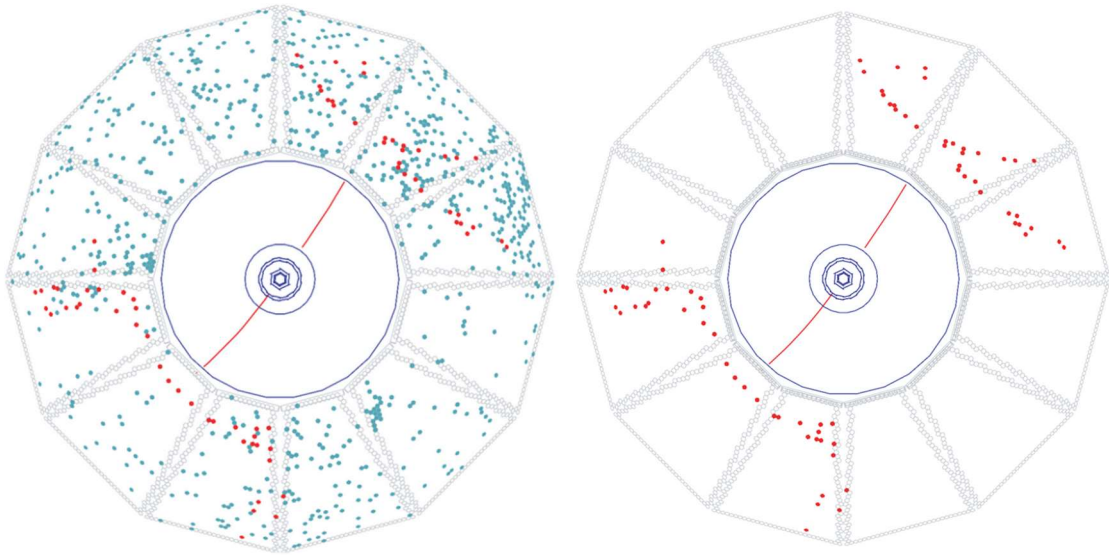
Figure 2.5: Display of the signals for a typical di-muon event for a $\pm 300\ ns$ trigger (left) and a $8\ ns$ trigger (right) [6].

2.4   The Electromagnetic Calorimeter

The electromagnetic calorimeter measures the electromagnetic showers that pass though the component within an energy range of 20 MeV to 9 GeV. Over this range the EMC can detect the photons from π^0 decays, η decays, electromagnetic processes, and from radiative processes. Further the EMC identifies electrons to aid in the flavor tagging of neutral B mesons in semi-leptonic decays. Otherwise, the identification of electrons aids in the measurements of rare decays of B and $D$ mesons alongside the τ lepton. The upper energy bound of the EMC leads from the necessity of measuring Quantum Electrodynamic (QED) processes such as $e^+e^- \rightarrow e^+e^-(\gamma)$ and $e^+e^- \rightarrow \gamma\gamma$ for calibrating the EMC. The lower energy bound comes from efficiently reconstructing the π^0 and η decays [5].

The EMC is a cylindrical barrel alongside a conical forward endcap. Within the EMC there are 6,580 CsI crystals separated into the barrel and the endcap. The barrel holds 5,760 crystals in 48 rings while the endcap has the remaining 820 crystals in eight rings. To decrease the effects of shower leakage from energetic particles the crystals increase in length from the backwards direction to the forward direction. To also limit pre-showering the crystals the outer radius support is only a thin gas seal at the front of the EMC [6].

To further describe the support structure for the crystals, the crystals are held in modules within the EMC that have their own support structure. There are three segments in the support structure, a cylinder for the barrel and two semi-circular structures for the endcap. The modules are comprised of 21 compartments for the barrel and 41 compartments for the endcap where each compartment holds one crystal. The compartments are made from

carbon-fiber epoxy composite with a wall thickness of 300 μm; additionally, the walls of the module are a further 300 μm thick for additional strength [6].

2.5   The Instrumented Flux Return

The instrumental flux return is the final segment of the Babar Detector and will identify the muons and neutral hadrons when working in tandem with the EMC. Detecting muons is important to appropriately tag the flavors of B decays via semi-leptonic decays. Further the IFR aids in vetoing charm decays alongside improving the reconstruction of neutrinos. The primary function of the IFR is to cover a large solid angle and to provide high background rejection for muons down to momenta below $1\,\mathrm{GeV/c}$ [5].

The IFR is built out of finely segmented steel and makes use of the steel flux return of the magnet as a muon filter and a hadron absorber. Further the detectors inside the steel are single gap resistive plate chambers (RPCs) with two-coordinate readout. The RPCs are installed into the gaps of the steel of the barrel and the end doors of the IFR. There are 18 segments to the steel of the IFR with each plate getting thicker from the innermost plate to the outermost plate. The barrel holds 19 RPC layers, and the end doors hold 18 RPC layers [6].

Chapter 3

Methods

The resonance particle $Y(4S)$, the Upsilon particle at 4S resonance, is a $b\bar{b}$ system at the 4S resonance with orbital momentum $\ell = 0$ (s-wave), in its 3rd radially excited state. The means of production and observation of $Y(4S)$ and its decays are explained in the previous chapter explaining the Babar Detector and PEP-II.

The specific decay process of interest is the neutral decay products of $Y(4S)$ into two neutral B and anti-neutral B meson pairs. To note when "on resonance" is used it describes the center of mass energy within the detector is at the $Y(4S)$ resonance of $10.58\ GeV$, and "off resonance" describes when the center of mass energy is just $40\ MeV$ below the $Y(4S)$ resonance. When resonance is achieved there are two decay paths that $Y(4S)$ could follow: either a pair of neutral B mesons ($Y(4S) \rightarrow B^0\overline{B^0}$) or a pair of charged B mesons ($Y(4S) \rightarrow B^+B^-$). In our current understanding of the Standard Model the likelihood of following either decay path for $Y(4S)$ is equal. Since the two options are equal the branching fraction for $Y(4S) \rightarrow B^0\overline{B^0}$, also known as f_{00}, is 0.50 [7, 8, 9]. However, from studies into the decay of $Y(4S)$ it has been realized that f_{00} should be less than 0.50 [2, 7, 8, 9, 10].

There are two decay chains for $Y(4S)$. As mentioned, that first decay chain produces two neutral B mesons, B^0 and $\overline{B}^0$. Taken from table 1.3, B^0 is comprised of a down quark and a bottom antiquark and $\overline{B}^0$ is comprised of a down antiquark and a bottom quark. Figure 3.1 shows the Feynman diagram for the pair of neutral B mesons from the decay of $Y(4S)$.
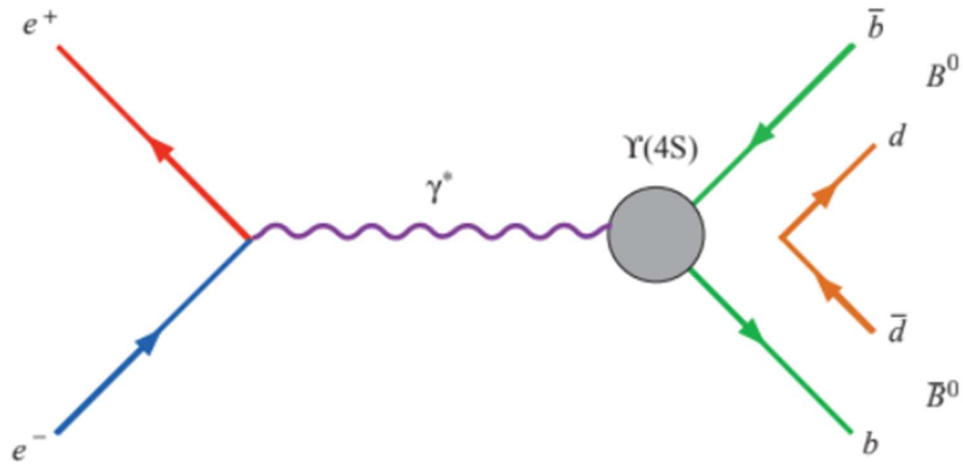
Figure 3.1: The Feynmann diagram representing the decay of $Y(4S)$

The alternative decay for $Y(4S)$ is the production of two charged B mesons B^+ and B^-. Once more referring to table 1.3, B^+ is comprised of an up quark and a bottom antiquark and B^- is comprised of an up antiquark and a bottom quark. For $Y(4S) \rightarrow B^+B^-$ the branching the fraction is known as f_{+-}. The ratio of these two branching fractions, the method at which the branching fractions has historically been measured, is denoted by $f_{+-}/f_{00} = R^{+/0}$. In previous studies the measurements of $R^{+/0}$ depended on the lifetimes of the charged and neutral B mesons alongside the isospin symmetry.

3.1 Full Reconstruction of B Mesons

The decay of the $\Upsilon(4S) \to B^0\overline{B^0}$ is not directly measured and instead it is the decay of the B mesons that are of interest. By detecting the decay products of the B mesons instead the B mesons from the decay of $\Upsilon(4S)$ can then be "observed." This process entails "reconstructing" the decay chains of the B mesons. It is through reconstruction that f_{00} will be calculated using the decay reconstruction of $\bar{B} \to D^{*+}\ell^-\bar{\nu}_\ell$.

The method of reconstruction relies upon identifying the stable daughter particles from the decay. As an example, the reconstruction of $\bar{B} \to D^{*+}\ell^-\bar{\nu}_\ell$ will look at the stable lepton and anti-lepton neutrino since these particles will not decay any further within the detector. It is noteworthy that the neutrino will not be detected by the detector, however. The reconstruction continues down to also reconstruct the D meson due to it no being a stable particle that has a short lifetime. Similarly to the B meson only the stable daughter particles are identified for the reconstruction of $D^{*+} \to D^0\pi^+$. So, the stable daughter particle identified is the pion while D^0 can be even further reconstructed as it decays further.

In reconstructing the D^0 meson all the daughter particles related to the original B meson will be identified except for the neutrino. This means of reconstruction is known as full reconstruction. Full reconstruction of B^0 is less effective due to Branching ratios reducing the total number of reconstructed D^0 mesons. So instead, a partial reconstruction technique will be employed in the determination of f_{00}.

3.2 Partial Reconstruction of B Mesons

As mentioned in full reconstruction all the daughter particles from the B meson decay are identified. In the full reconstruction the leptons and pions are stable enough to be detected but the D^0 mesons decays have a 5% branching ratio with respect to the decaying D^0 mesons.

As such the partial reconstruction technique does not reconstruct the D^0 mesons instead reconstructing the decay for $D^* \rightarrow D^0\pi^+$ through detection of pion. This leads to avoiding the reduced efficiency from reconstructing the D^0 mesons and improves the statistics for the yield by a factor of 20 [2]. The partial reconstruction technique has been applied once before in an analysis of f_{00} [2, 3] . For this current study, the sample size is approximately five times larger than the previous study mentioned leading to a reduction in statistical uncertainty.

The partial reconstruction technique relies on the fact that the D^* meson is massive enough to decay into a D^0 meson and a "soft" pion. The two decay products then have little momentum in the D^* meson's rest frame, hence the label of "soft" pion. As well as a low momentum in the D^* meson's rest frame the soft pion has a momentum less than 200 MeV/c in the $Y(4S)$ rest frame along the same direction as the parent D^*. The Decay path that partial reconstruction follows can be seen in Figure 3.2.
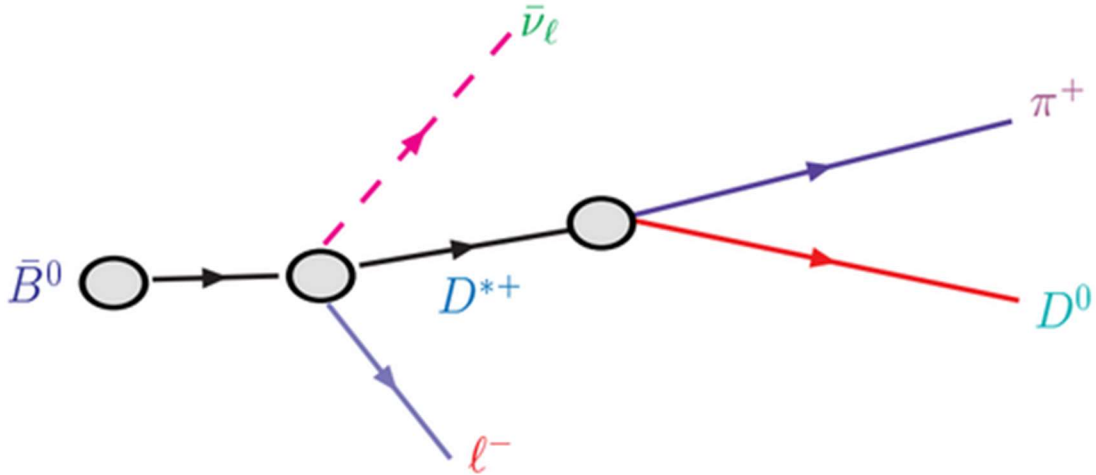
Figure 3.2: The decay path and the daughter particles identified through the partial reconstruction technique.

Using the soft pion's momentum, an approximation for the D^* four-momentum $(E_{D^*}^2, \tilde{\vec{p}}_{D^*})$ is found by scaling the soft pion's four-momentum according to Equation 3.1 and Equation 3.2. In these equations, E_π is the pion energy, $E_\pi^{cms} \approx 145 \; MeV$ is the energy of soft pion in the D^* rest frame, and $m_{D^*} = 2.01 \; GeV/c^2$ is the mass of the of the D^* meson [3].

$$E_{D^*} \simeq \frac{E_\pi}{E_\pi^{cms}} m_{D^*} \equiv \tilde{E}_{D^*} \, . \tag{3.1}$$

$$\vec{p}_{D^*} \simeq \widehat{\vec{p}_\pi} \times \sqrt{E_{D^*}^2 - m_{D^*}^2} \equiv \tilde{\vec{p}}_{D^*} \tag{3.2}$$

Where E_{D^*} and $\vec{p}_{D^*}$ are the energy and momentum of the D^* meson, $\widehat{\vec{p}_\pi}$ is the direction of the momentum of the pion, and $\tilde{E}_{D^*}$ and $\tilde{\vec{p}}_{D^*}$ are the approximate energy and momentum of

the D^* meson. To clarify, for partial reconstruction the particles used to reconstruct the $\bar{B}^0$ for the decay channel $\bar{B}^0 \to D^{*+}\ell^-\bar{\nu}_\ell (D^{*+} \to D^0\pi^+)$ are the lepton and the soft pion. Despite the neutrino being a stable daughter particle, it can not be used in reconstruction due to in negligible mass alongside being electrically neutral leads to it not being detected by the detector. Due to this, in the analysis of the conservation of momentum for the four-momentum of the $\bar{B}^0$ decay before and after the e^+e^- beam collision there is a certain amount of "missing mass" related to the neutrino in the decay. It is useful for this study to then report the events in terms of square of that mass known as "Missing Mass Squared." Since, as previously mentioned, the missing mass is from the undetected neutrino from the B meson decay it is labeled M_ν^2.

In the $Y(4S)$ rest frame the B meson has a small velocity allowing for relativistic effects to be ignored with a velocity to the speed of light ratio of $v/c = 0.065$ [11]. Beyond ignoring relativistic effects here, an approximation of the momentum of the B meson can be taken to be $\overrightarrow{P_B} \approx 0$. Using the energy and momentum conservation the value of M_ν^2 is:

$$M_\nu^2 \equiv \left(E_{beam} - \tilde{E}_{D^*} - E_\ell\right)^2 - \left(\tilde{\vec{p}}_{D^*} + \vec{p}_\ell\right)^2 \tag{3.3}$$

Where E_{beam} is the energy of the beam, $\tilde{E}_{D^*}$ is the energy of the D^* meson, E_ℓ is the energy of the lepton, $\tilde{\vec{p}}_{D^*}$ is the momentum of the D^* meson, and $\vec{p}_\ell$ is the momentum of the lepton. The missing mass squared for the partial reconstruction technique is the undetected neutrino. As such the missing mass squared distribution should peak around zero due to

the near zero mass of the neutrino. For the determination of the branching fraction f_{00}, the signal events are carefully extracted from several background events.

The analysis of the events is split into two types of data samples: the single tag events, and the double tag events. This is to reduce the necessary input of the efficiency reconstruction from the Monte Carlo simulations. Further the data has multiple "regions" that it falls into along the Missing Mass Squared distribution for the events. These regions are the signal region $-2.0\ GeV^2/c^4 < M_v^2 < +2.0\ GeV^2/c^4$ and the sideband region $-8.0\ GeV^2/c^4 < M_v^2 < -4.0\ GeV^2/c^4$. The negative missing mass squared happens when the momentum terms are greater than the energy terms.

The single tag events are any data sample with events that have at least one neutral B meson identified through partial reconstruction. The single tag events from the signal region are denoted by N_s. Similarly, the double tag events are any data sample with events that have both neutral B mesons identified through partial reconstruction. For an event to be labelled double tag the first candidate had to fall within the signal region, while the second candidate could be in the signal region. The double tag events from the signal region are denoted by N_d.

Using partial reconstruction, we can define the yield of both the single tag (N_s) and double tag (N_d) with Equation 3.4 and Equation 3.5, respectively [3].

$$N_s = 2N_{B\bar{B}} \times f_{00} \times \mathcal{B}(\bar{B}^0 \rightarrow D^{*+}\ell^-\bar{\nu}_\ell) \times \mathcal{B}(D^{*+} \rightarrow D^0\pi^+) \times \epsilon_s \qquad (3.4)$$

$$N_d = N_{B\bar{B}} \times f_{00} \times [\mathcal{B}(\bar{B}^0 \rightarrow D^{*+}\ell^-\bar{\nu}_\ell) \times \mathcal{B}(D^{*+} \rightarrow D^0\pi^+)]^2 \times \epsilon_d \qquad (3.5)$$

Where $N_{B\bar{B}}$ is the total number of $B\bar{B}$ events, ϵ_s and ϵ_d are the reconstructive efficiencies of the single tag and double tag events, respectively. The single tag events are doubled due to there always being to B mesons in the decay even when only one of the B mesons are reconstructed. Taking the ratio of the square of N_s and N_d and solving for f_{00} where the efficiency correlation between the single tag and double tag data is $C = \epsilon_d/\epsilon_s$ gives the branching fraction of $Y(4S) \rightarrow B^0\overline{B^0}$ [3]:

$$f_{00} = \frac{CN_s^2}{4N_dN_{B\bar{B}}} \tag{3.6}$$

The efficiency ratio of double tag and single tag events is checked with Monte Carlo samples and is taken to be approximately one.

3.3   Types of Backgrounds

As previously mentioned, the signal events need to be carefully extracted from backgrounds. The single and double tag data both have similar types of backgrounds: those being the continuum, combinatoric, and peaking backgrounds. The double tag sample, however, has two extra backgrounds known as the $M1_\nu^2$ combinatoric and the $M1_\nu^2$ peaking backgrounds. The continuum background is determined from the data while the remaining backgrounds are simulated using Monte Carlo.

The continuum background is from off resonance events, which are events that occurred when the center of mass energy of the e^+e^- beams where under the threshold for $Y(4S)$ production. These events, instead of $Y(4S)$ and its decay modes, produce hadrons of the form $e^+e^- \rightarrow q\bar{q}$ where $q = u, d, s$, or c leading to several possible hadrons. The created particles then disperse through the detector creating a spray of particles known as jets. These jets from the off-resonance events tend toward forming back-to-back jets in the detector; any jets of this form need to be removed. For on-resonance events the jets tend to express more isotropic in the $Y(4S)$ rest frame.

For efficiency continuum background events are reduced using the ratio $R_2 = H_2/H_0$ of the Fox-Wolfram moments [12]. This is achieved by requiring $R_2 < 0.5$ since jets with this ratio are more isotropic which increases the likelihood that these events are on-resonance. On the opposite side events that are closer to one are more likely to be back-to-back and thus off-resonance events. This requirement then reduces the contribution of off-resonance events by 50% without losing many $B\bar{B}$ events. The continuum background comes from the data and the number of these events is a small fraction of the total events, so this background is scaled by the ratio of the on-resonance and off-resonance luminosities and then directly subtracted off the data.

The peaking background comes from all the decays of type $\bar{B} \rightarrow D^* n(\pi)\ell^- \bar{\nu}_\ell$, where $n = 1, 2, \cdots$. This decay comes from the channels $B^- \rightarrow D^{*+} n(\pi)\ell^- \bar{\nu}_\ell$ and $\bar{B}^0 \rightarrow D^{*+} n(\pi)\ell^- \bar{\nu}_\ell$. A probable cause for the $D^* n(\pi)$ in the decay chain is the orbitally excited charm meson (D^{**}) dropping out of its excited state down to $D^* n(\pi)$. Beyond the orbitally excited charm meson there are three other possible contributors to the peaking background.

The first decay is $B^0 \rightarrow D^{*+}\pi^-$ where the pion is misidentified as a muon. The second decay is $B^0 \rightarrow D^{*+}\tau/X_c$ ($\tau/X_c \rightarrow \ell^-X$) where the daughter particles are either a lepton τ or a charmed hadron X_c that can further decay into another lepton-meson pair. The final decay is the radiative decay $\bar{B}^0 \rightarrow D^{*+}\gamma e^-\bar{\nu}_e$ where a photon γ is emitted. The leptons produced by each decay here is likely to have a lower momentum than the expected momentum of leptons in signal events thus having a high momentum cut-off of $1.5\ GeV/c$ reduces the contributions of the peaking background while reading the signal events. The three other decays that could contribute to the peaking background are treated as signal events in both single tag and double tag due to being very small but will have their effect considered in the systematic uncertainty.

Any other on-resonant, non-signal $B\bar{B}$ events that are not peaking background are referred to as combinatoric background. The combinatoric events are produced by a random combination of real leptons from B decays that are paired with the opposite charged soft pion that comes from the other B meson. Further the background could be contributed to by the low momentum soft pion that comes from the same or other B meson instead of the D^*.

For the double tag there are two other backgrounds alongside the above three backgrounds. The first is the $M1_\nu^2$ combinatoric background which occurs when the first candidate falls in the combinatoric background while the second candidate is in the signal. Similarly, the second background is the $M1_\nu^2$ peaking background which occurs when the first candidate falls in the peaking background while the second candidate is in the signal.

Chapter 4

Analysis

The previously described methods of measuring f_{00} will be shown in detail with the data represented by histograms of the event counts for a given interval of the Missing Mass Squared. To facilitate the plotting and manipulating the various histograms related to the data the main tool used is the C++ based plotting program Root. The fitting specifically will be performed by a Root fitting package called RooFit. The point of this analysis is to determine the total events that relate just to the Missing Mass Squared of the neutrino which cannot be reconstructed from the decay model. The total number of events related to the neutrino shall be referred to as the yield and is necessary to determining f_{00} using Equation 3.6. The analysis was performed once via subtraction of each respective background from the data to isolate the signal events and again via fitting all backgrounds to the data at once to determine the signal events as a check to the signal events from subtraction.

4.1 Subtraction of the Single Tag Events

To start the continuum background, as described in Chapter 3, is determined from the off-resonance data. The continuum background is scaled by the ratio of the luminosities of the on-resonance and off-resonance. After scaling this background is subtracted out prior to any further analysis of the yield. The remaining backgrounds are estimated using Monte Carlo before each background is subtracted out of the data leaving behind just the signal yield in the signal region.
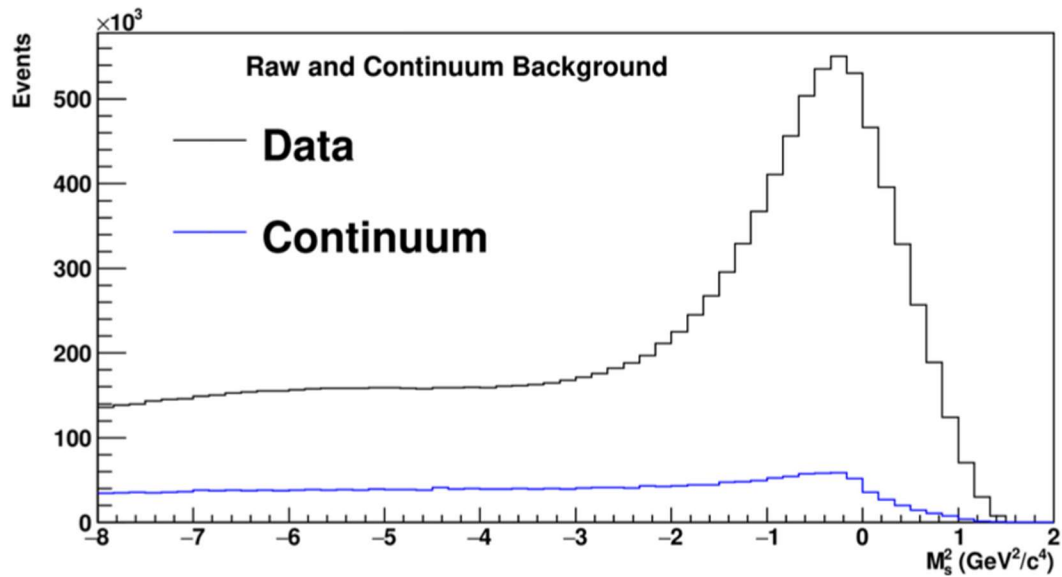

Figure 4.1: The continuum background plotted onto a histogram of the raw events for the Missing Mass Squared.

The data and the backgrounds are each in a histogram where the binning is the events measured for each Missing Mass Squared. This comes into focus for how the combinatoric background is handled. To remove the combinatoric background from the yield, the method of sideband subtraction is employed. Sideband subtraction entails taking the ratio

of the events of the continuum subtracted data and the events of the Monte Carlo continuum data in the sideband region. This scale is then used to extrapolate the combinatoric background into the signal region by scaling the Monte Carlo continuum data. After the scale, the combinatoric background histogram should line up with the sideband region events. This scaled histogram is then subtracted out of the data so that the sideband region's events are now around zero.
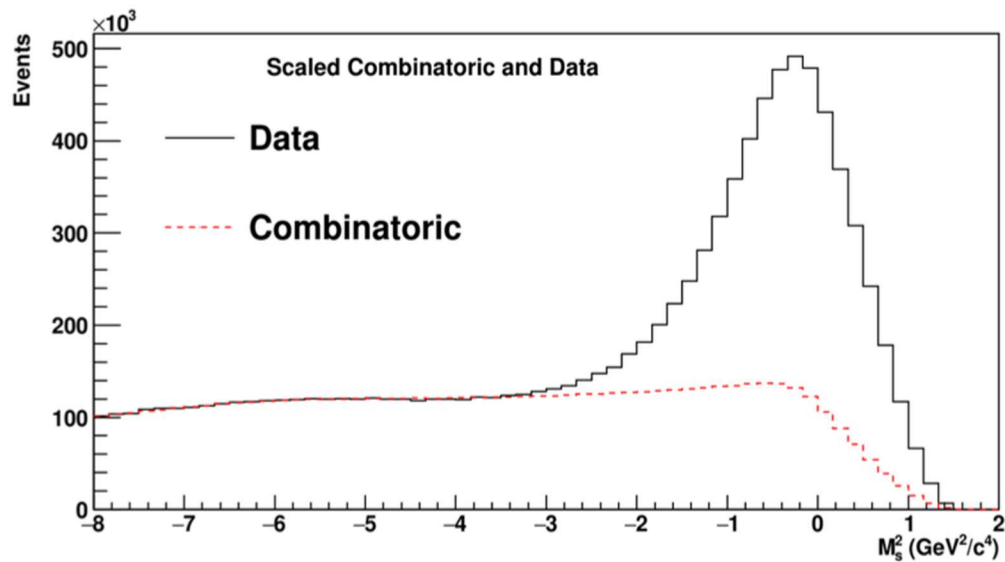

Figure 4.2: The combinatoric background scaled to the continuum subtracted data so the events in the sideband region match.

So now the last background to be subtracted from the data is the peaking background only in the signal region. The peaking background is estimated using the Monte Carlo for each of the four possible decays for both the $B^0\bar{B}^0$ events and the B^+B^- events for a total of eight histograms. For each possible decay, the Monte Carlo data is scaled by its isospin factor of $\frac{1}{3}$ for $B^0\bar{B}^0$ and $\frac{2}{3}$ for B^+B^- events. Then the Monte Carlo estimate of the peaking

background is these events summed together. Using the Monte Carlo events for the signal region the Monte Carlo data is scaled with the peaking data and then subtracted from the data. The remaining events is the yield N_s.

The number of events for each background is listed below in Table 4.3. Note that each number of events can be subtracted from the raw number of events to agree with the yield.
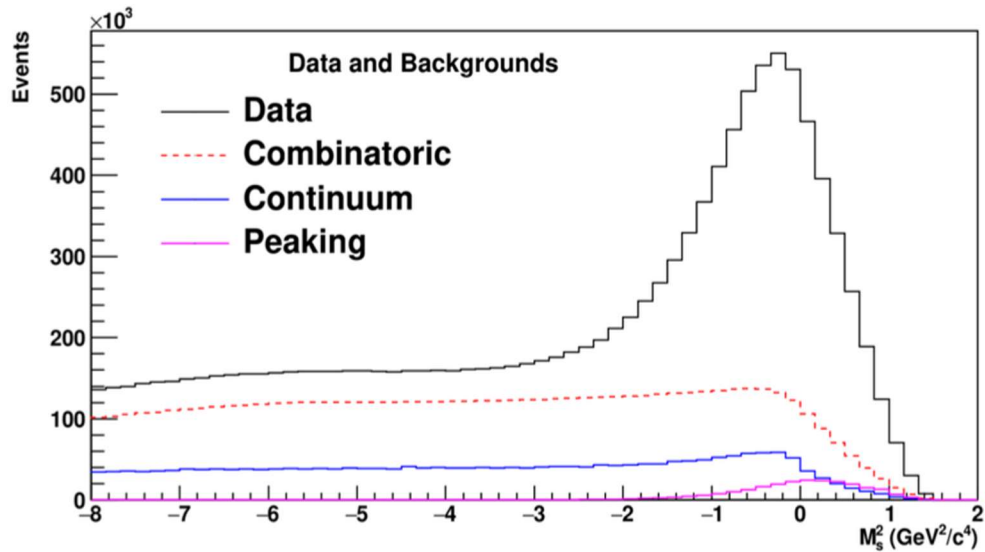

Figure 4.3: The continuum, combinatoric, and peaking backgrounds plotted onto a histogram of the data before subtraction occurs to determine the yield in the signal region.
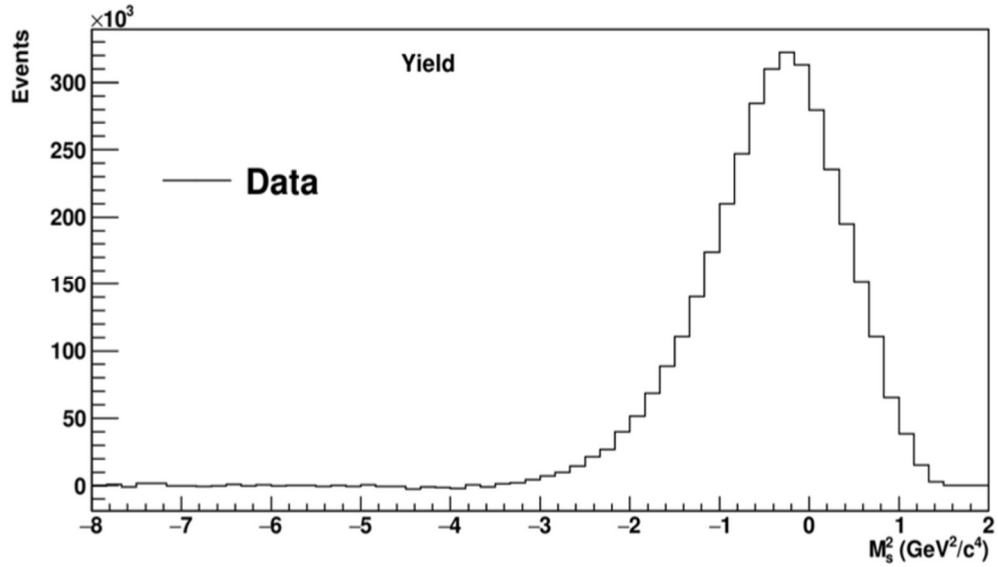
Figure 4.4: The final yield for the single tag, only events in the signal region remain as expected.

Table 4.1: The number of events for the data and the backgrounds subtracted to determine the yield in the signal region ($-2.0\ GeV^2/c^4 < M_v^2 < +2.0\ GeV^2/c^4$).

Source	Signal Region
Data	6586000 ± 2570
Continuum	732300 ± 855
Combinatoric	1989000 ± 1410
Peaking	445000 ± 926
Yield	3415000 ± 3190

4.2 Extracting the Single Tag Events through Fitting

As a consistency check for the analysis of the yield the previous analysis shall be performed via fitting the backgrounds to the data all at once instead of subtracting the backgrounds one at a time. The continuum background, however, is subtracted out of the data at the start before fitting in the same way as performed in the previous section. The Monte Carlo estimates for the combinatoric background, peaking background, and the signal of a sample which are then fit to the data using RooFit to extract the yield N_s.

The histograms for each background, the data, and the signal sample are supplied to RooFit where RooFit scales each histogram to the data histogram to "fit" them together. This then returns the number of events for each of the newly scaled histograms. Afterwards the ratio of the newly scaled events to the number of events of the original unscaled histograms can be found to determine scaling factors for each of the combinatoric background, the peaking background, and the Monte Carlo signal, respectively. These scaling factors are then applied to each respective background and the Monte Carlo signal.

Table 4.2: The single tag scaling factors for fitting the backgrounds and signal to data.

Source	Scaling Factor
Combinatoric	0.998
Peaking	2.12
Yield	1.03

After the scaling factors are applied to their respective background, each background can be displayed as a stack-one on top of the other to effectively "add" all of them together despite no summation occurring. This stack is then displayed on top of the continuum background, followed by the scaled Monte Carlo signal being stacked on top of scaled backgrounds. This summation of backgrounds alongside the Monte Carlo signal should then match to the distribution of the data. This is done by simply plotting the single tag data against the summed scaled background plus Monte Carlo signal. The performed fit is deemed correct when the stacked histograms match to the Single tag data as seen in Figure 4.5.
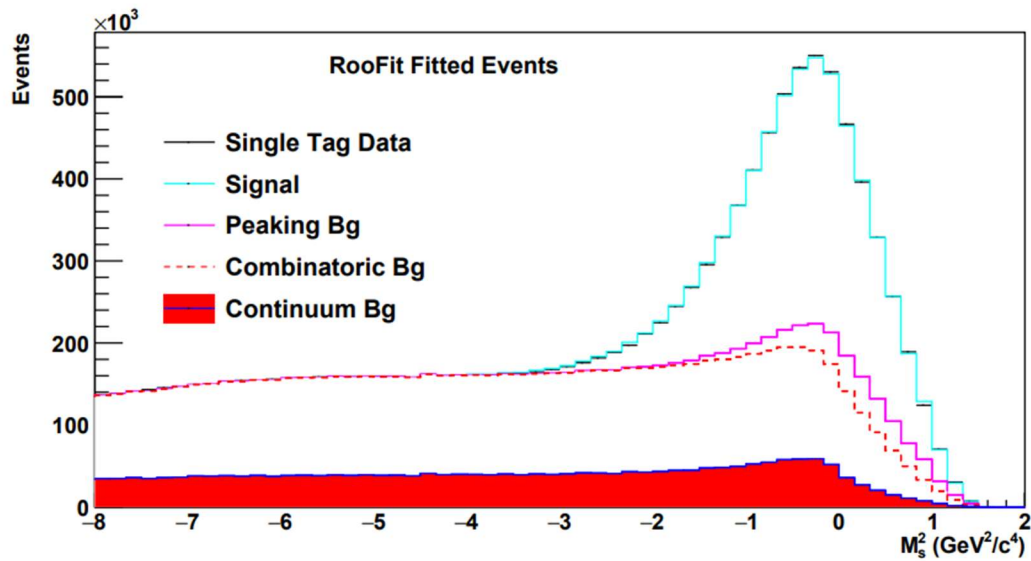

Figure 4.5: The fitted backgrounds and the signal stacked on top of each other plotted onto the single tag data, as seen the signal histogram matches with the single tag data nicely.

Table 4.3: The number of events from the fitting analysis for the backgrounds and the signal in the signal region ($-2.0\ GeV^2/c^4 < M_\nu^2 < +2.0\ GeV^2/c^4$).

Source	Signal Region
Data	6586000 ± 2570
Continuum	732300 ± 855
Combinatoric	1978000 ± 1410
Peaking	488400 ± 698
Yield	3386000 ± 3130

4.3   Subtraction of the Double Tag Events

The means of analyzing the double tag data follow much the same steps as the single tag data but also include analyzing the $M1_\nu^2$ combinatoric background and the $M1_\nu^2$ peaking background. The steps taken for the double tag subtraction for the backgrounds follows the same steps for the single tag. To start the continuum background is scaled by the ratio of the luminosities of on resonance to off resonance before subtracting it from the data. Followed by performing sideband-subtraction on the combinatoric background to remove it from the yield, bringing the sideband region to about zero events. Finally, estimating the peaking background using the Monte Carlo simulation of events from each of the possible decays that lend themselves to the peaking background and then scaling them to the peaking background. Afterwards, subtracting the peaking background from the data.
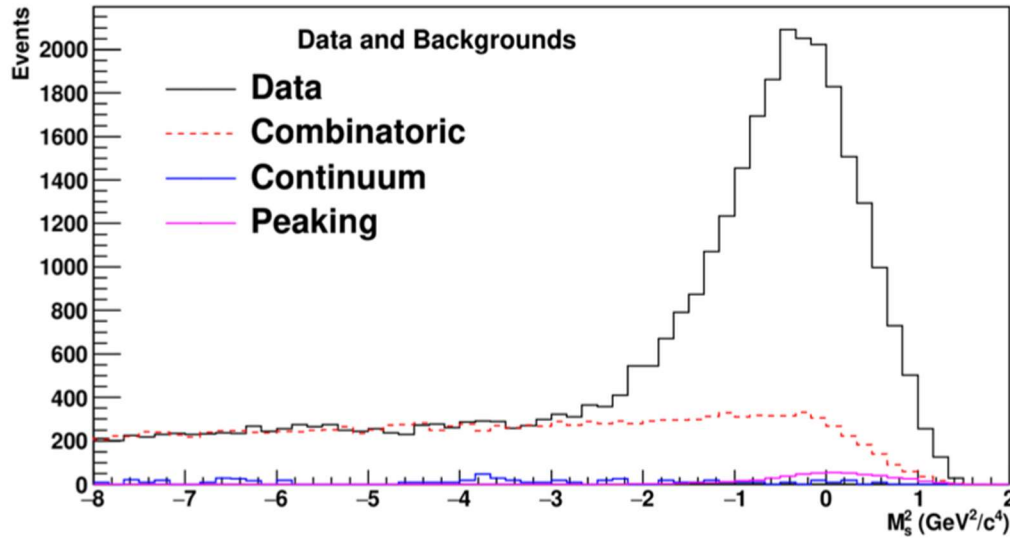
Figure 4.6: The continuum, combinatoric, and peaking backgrounds for the double tag events plotted onto the double tag data.

After performing the subtraction for the three previous backgrounds the remaining events are the signal events plus the event for the $M1^2_\nu$ combinatoric background and the $M1^2_\nu$ peaking background. To subtract out the $M1^2_\nu$ combinatoric background from the yield the method of sideband subtraction will also be used here like the combinatoric background. Here, however, the sideband subtraction is done over the right sign data using the wrong sign data to calculate the $M1^2_\nu$ combinatoric background itself. Right sign indicates that the detected lepton and soft pion hold the opposite electric charge to each other while wrong sign indicates that the detected lepton and soft pion hold the same electrical charge. To begin the right sign data and the wrong sign data for the $M1^2_\nu$ combinatoric background are estimated through the Monte Carlo. Then following sideband subtraction, the ratio of the sideband events of the right sign data to the wrong sign data is taken to scale the wrong

sign data to extrapolate it into the signal region. The scaled wrong sign data is then subtracted from the right sign data leaving the sideband region events around zero. The last step for the $M1_\nu^2$ combinatoric background is to scale the final histogram by two due to the two different lepton types the decay chain can have. This final histogram is now the $M1_\nu^2$ combinatoric background and can be subtracted out of the signal. The $M1_\nu^2$ peaking background then follows the exact same steps as the $M1_\nu^2$ combinatoric background except using the Monte Carlo estimations of the right sign and wrong sign data for the $M1_\nu^2$ peaking background. This final background too is subtracted out of the signal leaving just the yield for the double tag N_d.
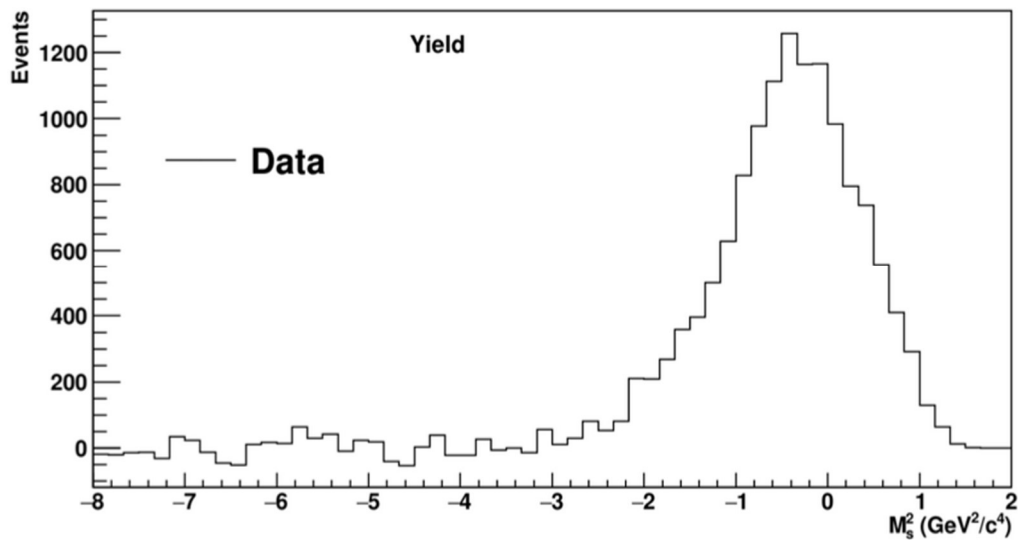

Figure 4.7: The yield for the double tag events with the continuum, combinatoric, peaking, $M1_\nu^2$ combinatoric, and $M1_\nu^2$ Peaking background subtracted out.

Table 4.4: The subtracted number of events for the double tag in the signal region $(-2.0 \; GeV^2/c^4 < M_\nu^2 < +2.0 \; GeV^2/c^4)$.

Source	Signal Region
Data	23630 ± 153
Continuum	153 ± 12
Combinatoric	4583 ± 66
Peaking	635 ± 28
$M1_\nu^2$ combinatoric	5306 ± 72
$M1_\nu^2$ peaking	104 ± 10
Yield	12850 ± 185

4.4 Extracting the Double Tag Events through Fitting

The same as the single tag the double tag will use the program RooFit to fit the backgrounds and the Monte Carlo signal to the data as a consistency check to the subtraction analysis. The double tag fitting analysis follows the same premise as the single tag fitting analysis but will also consider the double tags two extra backgrounds. The double tag data fitting analysis begins with subtracting the continuum background directly from the data before fitting; however, alongside the continuum background the $M1_\nu^2$ combinatoric background and the $M1_\nu^2$ peaking background will both also be subtracted out of the data prior to fitting. Both the $M1_\nu^2$ combinatoric background and the $M1_\nu^2$ peaking background will be determined using sideband subtraction between the respective, right sign and wrong sign data same as previous.

Once the Continuum, $M1_\nu^2$ combinatoric, and $M1_\nu^2$ peaking backgrounds ae subtracted out of the double tag data the two remaining backgrounds, combinatoric and peaking, alongside the Monte Carlo signal for the double tag data will be fit together through RooFit. Once again RooFit will scale up each of the bins for each of the input histograms to the double tag data giving the total number of events for each respective newly scaled histogram. The scaling factors for the backgrounds and the Monte Carlo signal are determined from the ratio of the number of events in the unscaled histogram to the scaled histogram. Afterwards, the original histograms are scaled by their respective scaling factors to determine each background and the signal.

Table 4.5: The double tag scaling factors for fitting the backgrounds and signal to data.

Source	Scaling Factor
Combinatoric	0.967
Peaking	1.21
Yield	0.844

With the scaled combinatoric and peaking backgrounds the two backgrounds can be displayed as a stack-one on top of the other to effectively "add" all of them together despite no summation occurring. This stack is then stacked on top of the continuum, $M1_\nu^2$ combinatoric, and $M1_\nu^2$ peaking backgrounds with the signal stacked on top of the two stacked backgrounds. These six stacked histograms are then overlayed onto the double tag data to determine their agreement. The summed backgrounds and signal together should match with the double tag data, if they do the fitting is correct as expressed in Figure 4.8.
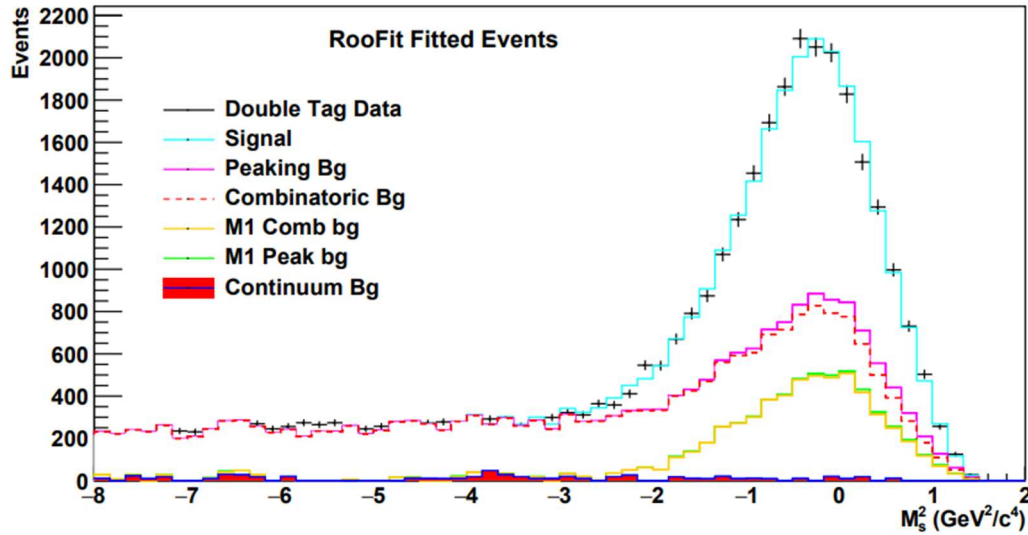
Figure 4.8: The fitted backgrounds and the signal stacked on top of each other plotted onto the double tag data, as seen the signal histogram matches with the double tag data nicely.

Table 4.6: The Fitted number of events for the double tag in the signal region $(-2.0\ GeV^2/c^4 < M_v^2 < +2.0\ GeV^2/c^4)$.

Source	Signal Region
Data	23630 ± 153
Continuum	153 ± 12
Combinatoric	4552 ± 67
Peaking	611 ± 24
$M1_v^2$ combinatoric	5306 ± 72
$M1_v^2$ peaking	104 ± 10
Yield	12910 ± 185

4.5   Determination of f_{00}

With the final yield for both the single and double tag analysis done through both counting statistics and fitting agreeing within 1% to the values found for N_s and N_d from the counting analysis can be used for the determination of f_{00}. The necessary values for solving Equation 3.6 are given in Table 4.7 alongside assuming $C \approx 1$.

Table 4.7: The number of events for both single and double tag data.

Source	Yield
N_s	3415000 ± 3190
N_d	12850 ± 185
$N_{B\bar{B}}$	$(4.674 \pm 0.0239) \times 10^8$

$$f_{00} = \frac{CN_s^2}{4N_d N_{B\bar{B}}} \tag{4.1}$$

Solving equation 3.6 gives the central value of the branching fraction of $Y(4S) \to B^0\overline{B^0}$ alongside analyzing the statistical uncertainty associated with the counting statistics in quadrature.

$$f_{00} = 0.485 \pm (0.007)_{Stat} \tag{4.2}$$

Chapter 5

Systematic Uncertainty

The statistical uncertainties related to each step of the analysis of f_{00} the has been given when appropriate. Beyond the statistical uncertainty associated with analyzing f_{00} there arises a systematic uncertainty too. The systematic uncertainty comes from a variety of sources within any experiment caused by physical limitations. These physical limitations could include sensitivity or efficiency of a detector or assumptions necessary to measurement. Secondary sources could be attributed to the Monte Carlo modeling of the experiment. For the determination of f_{00} the expected sources of systematic uncertainty accounted for are B counting, the peaking background, $\Upsilon(4S) \rightarrow$ non-$B\bar{B}$ events, MC modeling of combinatoric background, MC statistics, efficiency correlation, $M1_{\nu}^{2}$ combinatoric background, and $M1_{\nu}^{2}$ peaking background. The analysis of the systematic uncertainness will be explored within the following sections. Here the absolute systematic uncertainty of f_{00} is taken.

5.1 Sources of Systematic Uncertainties

The dominant systematic uncertainty in for the determination of f_{00} comes from the counting of the B mesons. This uncertainty is mainly attributed to the uncertainties within the tracking efficiency for measuring the particles. Further there is a statistical uncertainty related to the counting of the B mesons, however it is negligible compared to the systematic uncertainty and can be safely ignored. The current study the B counting systematic uncertainty is 0.6% [3].

The B counting systematic uncertainty is the impact of the non-$B\bar{B}$ decays of $Y(4S)$ counting the B mesons which is considered as another source of the systematic uncertainty. The branching fraction for the decay $Y(4S)$ to non-$B\bar{B}$ events is about 4% of the decays at the 95% confidence level. To determine the systematic uncertainty 50% of the upper limit branching fraction of the non-$B\bar{B}$ decays of $Y(4S)$ was taken. From this the systematic uncertainty for the non-$B\bar{B}$ decays of $Y(4S)$ is 0.2% [3].

The next systematic uncertainty comes from the efficiency correlation. The efficiency correlation is approximately one but is not quite one due to there being a small difference in the efficiency of the single and the double tag data. Since the two reconstruction efficiencies are slightly different, they do not become exactly one leading to systematic uncertainty. The systematic uncertainty is found through a track multiplicity study to directly measure the efficiency correlation and its contribution to the systematic uncertainty for f_{00}. The systematic uncertainty for the efficiency correlation is 0.2% [3].

5.2 Systematic Uncertainty Estimation

The remaining two systematic uncertainties are the systematic uncertainties related to the combinatoric and peaking backgrounds. Both uncertainties are analyzed making use of 1σ of the respective background in both the single and the double tag samples. To clarify 1σ is the statistical uncertainty associated to the whole data region, $-8\ GeV^2/C^4$ to $2\ GeV^2/C^4$, for the respective background. To determine the uncertainty, 1σ is added and subtracted from the background events to determine the percent difference between the original f_{00} value and the newly calculated f_{00} value from adding or subtracting 1σ.

For the combinatoric background the determination of the combinatoric itself comes from the Monte Carlo being scaled to the sideband of the data via sideband subtraction. The same steps will be applied here to determine the systematic uncertainty. The first step, however, is to add the statistical uncertainty from the whole region to the sideband and signal regions' number of events for the single tag data. These new values will then be used to calculate the new scaling factor for sideband subtraction and be used for sideband subtraction of the combinatoric background from the data. For the systematic uncertainty of the combinatoric background the continuum and peaking background events are held constant and are subtracted out in the same steps as described in the previous chapter.

This procedure is then followed again but this time by subtracting 1σ from the single tag and then twice more for adding and subtracting 1σ in the double tag data. Each respective yield will then be used to calculate a new f_{00} value. For each determination of f_{00} the respective new yield is used in place of the original while the other yield is held constant. As an example, for the determination of $+1\sigma$ from the single tag the double tag yield will

Table 5.1: The number of events after adding 1σ to the combinatoric events for the single tag events.

Source	Signal Region
Data	6586000 ± 2570
Continuum	732300 ± 855
Combinatoric	1990000 ± 1410
Peaking	450000 ± 926
Yield	3414000 ± 3190

the yield N_d from table 4.7. The f_{00} value is then compared to the central value to determine the percent difference caused by the change of 1σ to the background. The systematic uncertainty for the background is taken to be, conservatively, the percent difference of the greatest deviation from the standard value of the four.

Table 5.2: The yields for the combinatoric background for adding and subtracting 1σ and the percent difference for the central value of f_{00}.

Event Sample	Yield	f_{00}	$\delta f_{00}/f_{00}$ (%)
$+1\sigma$ Single tag	3414000	0.4852	0.04
-1σ Single tag	3415000	0.4856	0.04
$+1\sigma$ Double tag	12820	0.4862	0.20
-1σ Double tag	12870	0.4846	0.20

For the peaking background, a similar strategy is employed as the combinatoric background. The adding or subtracting of 1σ is applied directly to the peaking background events after the peaking background was already scaled as described in the previous chapter. This newly determined peaking background is then subtracted from the data for the new yield which is used to redetermine f_{00} for its four new values. From there the same steps are applied to determine the percentage of the systematic uncertainty from the largest deviation from the central value.

Table 5.3: The yields for the peaking background for adding and subtracting 1σ and the percent difference for the central value of f_{00}.

Event Sample	Yield	f_{00}	$\delta f_{00}/f_{00}$ (%)
$+1\sigma$ Single tag	3414000	0.4852	0.06
-1σ Single tag	3416000	0.4857	0.05
$+1\sigma$ Double tag	12820	0.4865	0.20
-1σ Double tag	12880	0.4844	0.20

The determination of the systematic uncertainty itself comes from summing each of the percent errors together in quadrature. All contributions to the systematic uncertainty are listed in table 5.4.

Table 5.4: The percentage difference to the central value for each contribution to the systematic uncertainty.

Source	$\delta f_{00}/f_{00}$ (%)
B counting	0.6
$\Upsilon(4S) \to$ non-$B\bar{B}$	0.2
MC Statistics	0.2
Efficiency correlation	0.2
$M1_\nu^2$ combinatoric	0.1
$M1_\nu^2$ peaking backgrounds	0.1
Combinatoric background	0.2
Peaking background	0.2
Total systematic uncertainty	0.8

Once the uncertainties are summed together in quadrature the final percentage is taken as the full contribution to the systematic uncertainty.

$$f_{00} = 0.485 \pm (0.007)_{Stat} \pm (0.004)_{syst} \qquad (5.1)$$

where the first uncertainty is statistical and the second is the systematic uncertainty.

Conclusion

This analysis is a first model independent measurement of the branching fraction of $\Upsilon(4S) \to B^0\overline{B^0}$, f_{00}, with partial reconstruction of $\overline{B}^0 \to D^{*+}\ell^-\bar{\nu}_\ell$. It is a direct experimental measurement of $\Upsilon(4S) \to B^0\overline{B^0}$ that is independent of $\overline{B}^0$ lifetime as well as the branching fractions of $\overline{B}^0$ and D^{*+}.

Based on a data sample of 476 million B-meson anti-B-meson pairs collected at the $\Upsilon(4S)$ resonance with the BABAR detector at the PEP-II asymmetric-energy B-Factory at SLAC, we measure the branching fraction of $\Upsilon(4S) \to B^0\overline{B^0}$.

$$f_{00} = 0.485 \pm (0.007)_{Stat} \pm (0.004)_{syst} \tag{5.2}$$

Where the first uncertainty is statistical and the second is the systematic uncertainty. This result is better in precision compared to the present world average.

Our result does not depend on any branching fractions, the simulated reconstruction efficiency, the ratio of the charged and neutral B meson lifetimes, or assumption of isospin symmetry. A precision measurement of f_{00} or f_{+-} will allow an absolute renormalization of all B meson branching fractions and important for understanding the magnitude of isospin violating effects in $\Upsilon(4S) \to B^0\overline{B^0}$.

References

[1] R.L. Workman *et al.* (Particle Data Group), Prog.Theor.Exp.Phys., 083C01 (2022).

[2] BABAR Collaboration, B. Aubert *et al.*, Phys. Rev. Lett. 95, 042001 (2005).

[3] R. Godang, L. Cremaldi, and D. Summers, BABAR Analysis Document 731 (2005)

[4] BABAR Collaboration, The BABAR Physics Book SLAC-R-504 74, (1998).

[5] BABAR Collaboration, The BABAR Physics Book SLAC-R-504 78-104, (1998).

[6] BABAR Collaboration, B. Aubert *et al.,* Nucl. Instrum. Meth. A 479, 1 (2002).

[7] CLEO Collaboration, B. Barish *et al.*, Phys. Rev. D 51, 1014 (1995).

[8] BABAR Collaboration, B. Aubert *et al.*, Phys. Rev. D 65, 032001 (2002).

[9] CLEO Collaboration, S.B Athar *et al.*, Phys. Rev. D. 66, 052003 (2002).

[10] D Scora and N. Isgur, Phys. Rev. D 52, 2783 (1995).

[11] R. Kaiser, A.V. Manohar, and T. Mehen, Phys. Rev. Lett. 90, 142001 (2003).

[12] G.C. Fox and S. Wolfram, Phys. Rev. Lett. 41, 1581 (1978).

Vita

Daniel B. Johnson was born on May 18, 2002, to Jamie N. Johnson and Jaysn J. Johnson.

Raised in Mobile, Alabama, he graduated from Baker High School, class of 2020.

He will graduate from the University of South Alabama, Honors College class of 2024,

with his Bachelor of Science in Physics and a Bachelor of Science in Mathematics.

In Fall 2024, he will begin graduate studies at the Department of Physics and Astronomy

at the University of Alabama in Huntsville.